Predictability of a Coupled Model of ENSO Using Singular Vector Analysis. Part I: Optimal Growth in Seasonal Background and ENSO Cycles

YAN XUE,* M. A. CANE, AND S. E. ZEBIAK

Lamont-Doherty Earth Observatory, Columbia University, Palisades, New York

(Manuscript received 5 February 1996, in final form 16 December 1996)

ABSTRACT

The fastest initial error growth (optimal growth) in the Zebiak and Cane (ZC) forecast model for the El Niño–Southern Oscillation (ENSO) is analyzed by singular value decomposition of a forward tangent model along a trajectory in a reduced EOF space. In this paper (Part I of II), optimal growth about the seasonally varying background and ENSO cycles from a long model run are discussed.

Among the many forms of nonlinearity in ZC, the discontinuity of the slope in subsurface temperature at zero thermocline depth and the nonlinear advection of SST are the most significant. That positive perturbations grow much faster than negative perturbations around the seasonally varying background is first attributable to the discontinuity and, second, attributable to nonlinear advection.

About the seasonally varying background, 6-month optimal growth is largest for early (boreal) spring starts, which is related to the enhanced atmospheric heating due to equatorward movement of the ITCZ. One dominant growing structure is found, characterized by north–south and east–west SST dipoles, convergent winds on the equator in the eastern Pacific, and a deepened thermocline in the whole equatorial belt. This structure is insensitive to start month and optimization time.

Optimal growth about ENSO cycles in a long model run is generally much smaller than that about the seasonally varying background. As before, one dominant growing structure, insensitive to start time and optimization time, is found. During the warm phase of ENSO, optimal growth is modulated by season as is that about the seasonal varying background. During the onset and mature phases of ENSO, the final pattern of the optimal structure in 6 months is confined to the eastern Pacific; during the decay phase of ENSO, it spreads to the western Pacific as well. During the cold phase of ENSO, optimal growth has two maxima in a year—early spring and fall; the optimal perturbation propagates westward associated with surface layer–wind interaction.

The authors also compare the singular vector analysis in EOF space and the standard one in physical space. The importance of norm definition to optimal growth and optimal structure is discussed.

1. Introduction

In the past decade, the El Niño and the Southern Oscillation (ENSO) phenomenon has received tremendous attention. Models ranging from simple analytical ones, through intermediate coupled numerical models, to sophisticated coupled GCMs have simulated ENSO with varying successes and have offered different theories for its origin [see the review by McCreary and Anderson (1991)]. Although some numerical models, such as that of Zebiak and Cane (Cane et al. 1986; Zebiak and Cane 1987) and the coupled GCM at the National Centers for Environmental Prediction (Ji et al. 1994), have simulated the real ENSO system quite well in the past decade, discrepancies between models and reality remain (see the review by Latif et al. 1994). Because of poor data coverage in the tropical Pacific, these models are almost certainly not well initialized. It is hence unclear whether errors in the models, or errors in the models' initial fields, are the primary limitation. Here we focus on the initial error growth in the Zebiak and Cane (1987) model (hereafter ZC) and explore how it varies with the initial states.

Weather prediction skill is well known to be state dependent. Lorenz (1965) first pointed out that the fastest error growth rate, measured by the largest singular value of a forward tangent model, may vary by an order of magnitude due to changes in initial states. This type of growth exists in a non-self-adjoint system and has been studied extensively in recent years (Lacarra and Talagrand 1988; Farrell 1989; Molteni and Palmer 1993; Palmer et al. 1994; Buizza and Palmer 1995). For synoptic-scale circulations the largest singular value can be used as an appropriate warning of uncertainties in numerical weather prediction. More realistic ensemble forecasts are now being constructed using the fastest-

* Current affiliation: National Centers for Environmental Prediction, Camp Springs, Maryland.

Corresponding author address: Dr. Yan Xue, NCEP, Room 807, WWB, 5200 Auth Road, Camp Springs, MD 20746.
E-mail: wd01yx@sun1.wwb.noaa.gov

growing singular vectors as initial perturbations in numerical weather forecasts at the European Centre for Medium-Range Weather Forecasts (Mureau et al. 1993; Molteni et al. 1996).

Using a Markov model based on ZC, Blumenthal (1991) pointed out that the ENSO system is non-self-adjoint, exhibiting fast transient growth even though all principal oscillation patterns decay. Xue et al (1994) further showed that the transient growth is seasonal and that the model's prediction skill is related to the non-self-adjoint error growth. The models used by Blumenthal (1991) and Xue et al. (1994) are statistical reductions of ZC, which can describe only the seasonal variation of error growth. However, both the model and real system have error growth that depends not only on season, but also on the states of ENSO. Here we will use the method of Lorenz (1965) to address this issue. Considering the limited number of structures that are supported in the ZC model, for ease and efficiency, we choose to construct the required forward tangent models in a reduced EOF space.

The results will be presented in two parts. Part I (this paper) introduces the theory of singular vector analysis and the methodology of constructing a forward tangent model in EOF space. Then the perturbation growth about the seasonal background and interannually varying states is studied. Part I serves as a guidance and basis for Part II (Xue et al. 1997). The goal of Part II is to use the tool of singular vector analysis to understand the ZC model's forecast skill over the past two decades.

There are six sections in Part I. The next section concerns the construction of a forward tangent model and the formalism of singular vector analysis and, for comparison, also reviews the construction of Markov model. Section 3 contains the singular vector analysis about the seasonally varying background. The influence of the interannual variability on perturbation growth is studied in section 4. Section 5 discusses the sensitivity of the growth rate to different variables and the important role of norm definition. Section 6 presents a summary and conclusions.

2. Forward tangent model and singular vector analysis

a. EOF reduction

Following is a brief summary of the model variables. Details may be found in Cane and Patton (1984) and Zebiak and Cane (1987). The model describes anomalies about a specified, seasonally varying, background. The oceanic component of the ZC model describes a linear, single baroclinic mode combined with a surface mixed layer. The SST equation in the surface mixed layer is fully nonlinear, including advection by both mean currents and anomalous currents. SST variations do not affect the ocean dynamics. The atmospheric model dynamics describes a linear flow with vertical structure given by a single baroclinic mode. The atmospheric anomalous heating is prescribed in terms of SST anomalies, plus a wind convergence feedback (Zebiak 1986). The atmospheric heating due to the convergence feedback is determined interactively using up to three iterations. For computational efficiency, the atmospheric wind anomaly (Ua, Va), the wind convergence anomaly (D), and heating anomaly (Q) from the previous time step are used in the first iteration at each time step. Because the atmospheric solution is not iterated to complete convergence, the variables Ua, Va, D, and Q are not exactly derivable from SST alone. Therefore the oceanic dynamic variables, thermocline depth (H), zonal (U), and meridional (V) currents, plus SST, Ua, Va, D, and Q are used in constructing forward tangent models.

Since the dimension of the oceanic dynamic variables is on the order of 10^4, building a forward tangent model in physical space demands tremendous computation. A way to avoid the expensive computation is to build an adjoint tangent model. Considering that the model supports only a limited number of EOF modes, it is advantageous to build a forward tangent model in a reduced EOF space. Our assumption is that the initial error fields can be well described by the limited number of EOF modes. Presumably the forward tangent model in a reduced EOF space can be as accurate as possible when the EOF space expands sufficiently. Some authors have chosen to look at the SST optimal alone (Chen et al. 1997). However, the goal of singular vector analysis is to find the optimal growing errors in analyses, and assuming analysis errors in SST alone is limiting. Forward tangent models in a reduced EOF space spanning all model variables are more suitable for this purpose. In addition, an appropriate norm definition that describes a white error field is essential. For a white initial error covariance, the initial errors are distributed uniformly among all the singular vectors, so that the components of the fast-growing singular vectors will dominate the initial error growth.

A suite of 2-yr runs starting from the model initial fields in the ZC standard forecasts for each month between January 1970 and December 1993 was carried out. The fields (H, U, V, SST, Ua, Va, D, and Q) were saved once per month, yielding a dataset with $24 \times 12 \times 25$ monthly values. An EOF analysis was applied to each variable. Keeping 96, 149, 209, 37, 11, 17, 42, and 16 EOFs of H, U, V, SST, Ua, Va, D, and Q, respectively, allowed at least 91% of the variance of the model initial fields and 95% of the variance of the model forecast fields to be represented.

Next the principal components (PCs) for each variable were combined to form a new state vector, and a second EOF analysis was performed to further reduce the state space. Since these state fields are from different components of the coupled model and have different physical units, proper scaling or weighting factors among them are needed. We divided the state fields into

four groups: *H*, *U*, and *V* form one group; SST another; Ua and Va another; *D* and *Q* another. Since there is no prior knowledge about the weighting factors between the groups, a weighting factor of 1 is given to the oceanic, SST, and atmospheric wind groups, but a weighting factor $\varepsilon = 0.01$ is given to the group of convergence and heating anomaly. We assume that the latter two variables are closely correlated with SST and wind. Assigning them a low weight means that they do not affect the multivariate EOF selection, while allowing the software to find their associated structures. The new state vector constructed from the PCs of *H*, *U*, *V*, SST, Ua, Va, *D*, and *Q* is

$$\mathbf{b} = \left(\frac{\mathbf{a}_H}{\sigma_O}, \frac{\mathbf{a}_U}{\sigma_O}, \frac{\mathbf{a}_V}{\sigma_O}, \frac{\mathbf{a}_{\rm SST}}{\sigma_{\rm SST}}, \frac{\mathbf{a}_{Ua}}{\sigma_W}, \frac{\mathbf{a}_{Va}}{\sigma_W}, \varepsilon\frac{\mathbf{a}_D}{\sigma_D}, \varepsilon\frac{\mathbf{a}_Q}{\sigma_Q}\right)^{\rm T}. \quad (1)$$

Here $\mathbf{a}_H$, $\mathbf{a}_U$, $\mathbf{a}_V$, $\mathbf{a}_{\rm SST}$, $\mathbf{a}_{Ua}$, $\mathbf{a}_{Va}$, $\mathbf{a}_D$, and $\mathbf{a}_Q$ are the PCs of *H*, *U*, *V*, SST, Ua, Va, *D*, and *Q* with dimensions 149, 96, 209, 37, 11, 17, 42, and 16, respectively; σ_O is the total variance described by the PCs of *H*, *U*, and *V*,

$$\sigma_O^2 = \sum_t \left[\|\mathbf{a}_H(t)\|^2 + \|\mathbf{a}_U(t)\|^2 + \|\mathbf{a}_V(t)\|^2\right], \quad (2)$$

which is also the energy of the ocean model since *H*, *U*, and *V* have been nondimensionalized (refer to Cane and Patton 1984); $\sigma_{\rm SST}^2$ is the total variance described by the PCs of SST; σ_W^2 is the total variance described by the PCs of Ua and Va; σ_D^2 is the total variance described by the PCs of D; and σ_Q^2 is the total variance described by the PCs of *Q*. The vector $\mathbf{b}$ is subject to a second EOF analysis. Then the state vector in physical space spanning the eight fields (designated $\mathbf{q}$) is decomposed into space function matrix $\mathbf{E}$ and time series $\mathbf{c}$, that is,

$$\mathbf{q} = \mathbf{E}\mathbf{c}, \quad (3)$$

where $\mathbf{E}$ is orthogonal with respect to $\mathbf{W}$,

$$\mathbf{W} = \text{diag}\left(\frac{1}{\sigma_O^2}, \frac{1}{\sigma_O^2}, \frac{1}{\sigma_O^2}, \frac{1}{\sigma_{\rm SST}^2}, \frac{1}{\sigma_W^2}, \frac{\varepsilon^2}{\sigma_D^2}, \frac{\varepsilon^2}{\sigma_Q^2}\right); \quad (4)$$

that is

$$\mathbf{E}^{\rm T}\mathbf{W}\mathbf{E} = \mathbf{I}. \quad (5)$$

b. Forward tangent model and singular vector analysis

The method for constructing a forward tangent model is similar to that in Lorenz (1965). Suppose $\mathbf{z}^t$ is the state vector at time *t*, $\mathbf{z}^{t+1}$ is the vector at time $t+1$, and that they are related through the full nonlinear model *A*,

$$\mathbf{z}^{t+1} = A(\mathbf{z}^t). \quad (6)$$

If a small perturbation in the *j*th multivariate EOF, $\varepsilon\mathbf{e}_j$, is added to $\mathbf{z}^t$, the new state vector at time $t+1$, $\mathbf{z}^{t+1'}$, is given by

$$\mathbf{z}^{t+1'} = A(\mathbf{z}^t + \varepsilon\mathbf{e}_j) = \mathbf{z}^{t+1} + \frac{\partial A}{\partial \mathbf{e}_j}\varepsilon\mathbf{e}_j + O(\varepsilon^2). \quad (7)$$

Expanding the perturbation at time $t+1$ into multivariate EOFs gives $\mathbf{z}^{t+1'} - \mathbf{z}^{t+1} = \Sigma\mathbf{e}_k d_k$, where

$$\sum \mathbf{e}_k d_k = \frac{\partial A}{\partial \mathbf{e}_j}\varepsilon\mathbf{e}_j + O(\varepsilon^2). \quad (8)$$

Multiplying by $\mathbf{e}_k^{\rm T}\mathbf{W}$ on both sides of Eq. (8) and neglecting the higher order of perturbations yields

$$\mathbf{e}_k^{\rm T}\mathbf{W}\frac{\partial A}{\partial \mathbf{e}_j}\mathbf{e}_j = \frac{d_k}{\varepsilon}, \quad (9)$$

where we have invoked the orthogonality of $\{\mathbf{e}_k\}$ [refer to Eq. (5)]. Here, $\mathbf{L}_{k,j} \equiv \mathbf{e}_k^{\rm T}\mathbf{W}(\partial A/\partial \mathbf{e}_j)\mathbf{e}_j$ is the *j*th column of the forward tangent model $\mathbf{L}$. By varying *j* from 1 to *N*, the forward tangent model $\mathbf{L}$ for the interval t to t+1 about the control run trajectory $\mathbf{z}^t$ in the *N*-dimensional EOF space is obtained. The results presented in this paper were obtained using $N = 50$. We have repeated most of the calculations with $N = 100$; similar results are found, and all the conclusions in the paper are unchanged.

Considering the nonlinear advection in the SST equation and the several model ''switches'' (e.g., in the atmospheric convergence feedback and the vertical temperature advection in SST equation), we initially used a time step of 10 days (the same as the oceanic dynamics) to construct a forward tangent model $\mathbf{L}$ and checked its convergence by gradually decreasing ε. It was found that numerous fast-decaying modes are generated in 10 days, but the EOF space structures $\mathbf{E}$ calculated from the monthly data do not necessarily span them. Since we only need to approximate the ZC model with a forward tangent model on monthly and longer timescales, which are relevant to ENSO, we subsequently chose a 1-month time step to build the transition matrix $\mathbf{L}$.

To test whether a unique forward tangent model was obtained, we compared the largest singular values of the two transition matrices constructed using positive and negative perturbations. It was found that when the perturbation $\varepsilon\mathbf{e}_j$ has less than 0.1% of the variance of the model fields, the two transition matrices calculated from $\varepsilon\mathbf{e}_j$ and $-\varepsilon\mathbf{e}_j$ are in good agreement. The averaged difference of the largest singular values of the 1-month transition matrices is less than 5%.

The transition matrix $\mathbf{L}_\tau$ for an interval of τ months is the multiplication of τ 1-month transition matrices. We used the L_2 norm to calculate singular vectors of $\mathbf{L}_\tau$. This norm in the multivariate EOF space represents the sum of the variance (normalized) of the oceanic currents, thermocline depth, SST, and wind anomalies while taking little notice of the variance of the divergence and heating anomalies. The singular vectors $\mathbf{u}_j$ of $\mathbf{L}_\tau$ are the eigenvectors of $\mathbf{L}_\tau^{\rm T}\mathbf{L}_\tau$ (Strang 1988):

$$\mathbf{L}_\tau^{\rm T}\mathbf{L}_\tau\mathbf{u}_j = \sigma_j^2\mathbf{u}_j, \quad (10)$$

where σ_j are the singular values. By definition, the tran-

sition matrix $\mathbf{L}_\tau$, as well as its singular vectors and singular values, vary with initial time and evolution interval τ.

Blumenthal (1991) computed a Markov model by using a single-step covariance matrix. The least square best fit, $\mathbf{M}$, to the model data $\mathbf{c}(t)$ in Eq. (3), satisfies

$$\mathbf{M} = \langle \mathbf{c}(t+1)\mathbf{c}(t)^{\mathrm{T}} \rangle \langle \mathbf{c}(t)\mathbf{c}(t)^{\mathrm{T}} \rangle^{-1}. \quad (11)$$

By construction, the Markov model is an averaged linear model among all model states (see Blumenthal 1991). It is a linear approximation to ZC for a 1-month time step and describes the total model fields as opposed to perturbation fields described by forward tangent models.

Forward tangent models are built about a control run trajectory. They vary with initial state and describe only small perturbation growth along the trajectory. If the ZC model were strictly linear, the Markov model (if the samples for the Markov calculation are long enough) and the forward tangent model would be identical. Since in reality the ZC model is quite nonlinear, the two models are at times quite different. This point will be explored further below.

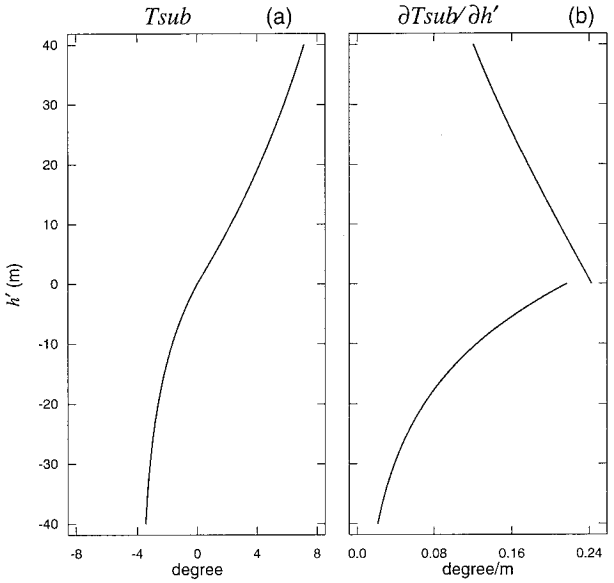

FIG. 1. (a) The subsurface temperature and (b) the subsurface temperature slope as functions of thermocline depth anomaly at 90°W.

3. Seasonal background state

There are many nonlinear terms in ZC, the most important being the nonlinear advection in the SST equation, the subsurface temperature parameterization, and the wind stress formulation. Various switches in the model (relating to the atmospheric convergence feedback and mixed layer vertical temperature advection) also produce nonlinearity (Zebiak and Cane 1987). However, many of the switches are only turned on occasionally, and the model's short-term behavior is well determined by large-scale structures irrespective of them. Two others that have greater impact—one a limit of 30°C on total SST, and another concerning ''reinitialization'' of the atmospheric model (see ZC)—were excluded in the tangent model calculation. We verified that neither of them is important for forecasting, in the sense that none of them appreciably affects the ZC's prediction skill over the verification period from 1972 to 1995.

For the seasonal background state, the discontinuity in the slope of the subsurface temperature is also a problem for constructing forward tangent models. The subsurface temperature parameterization is

$$T_{\mathrm{SUB}} = \begin{cases} T_1\{\tanh[b_1(\bar{h} + h')] - \tanh(b_1\bar{h})\}, & h' \geq 0; \\ T_2\{\tanh[b_2(\bar{h} + h')] - \tanh(b_2\bar{h})\}, & h' < 0. \end{cases} \quad (12)$$

Here $T_1 = 28$°C, $b_1 = (80\ \mathrm{m})^{-1}$, and $T_2 = -40$°C, $b_2 = (33\ \mathrm{m})^{-1}$; $\bar{h}$, h' are the mean and anomalous thermocline depths; and T_{SUB} is the temperature anomaly at the bottom of the mixed layer. A positive thermocline depth anomaly gives a much larger subsurface temperature signal than does an equal magnitude negative anomaly (Fig. 1a). This is evidently true in nature as well. The slope of T_{SUB} at a positive thermocline depth anomaly is much larger than that at the same amplitude of negative thermocline depth anomaly (Fig. 1b). The discontinuity at zero implies very strong nonlinearity. It is modified to be symmetric for warm and cold anomalies by taking $T_1 = -T_2 = 28$°C and $b_1 = b_2 = (80\ \mathrm{m})^{-1}$. Then a unique tangent model is obtainable.

For each start month, monthly forward tangent models are constructed using the Lorenz method (section 2). We used both positive and negative perturbations in constructing the forward tangent models. It is found that the first singular values of the monthly forward tangent models from positive and negative perturbations differ by less than 1% if the perturbation ε is less than 0.1% of the mean variance.

Figure 2 shows the first and second singular values optimized at 1, 3, and 6 months as functions of start month. It is seen that the first singular value optimized at 6 months is at least twice of the second singular value. Subsequently we discuss only the first singular value and vector. The first singular value optimized at 3 months indicates the northern spring and summer as favorable growth seasons. Tziperman et al. (1997) have studied the seasonal evolution of ENSO in ZC and found that the most dominant seasonal modulation is due to the wind divergence field, as determined by the seasonal motion of the ITCZ, through its effect on the atmospheric heating. They pointed out that the annual mean background is stable, itself unable to sustain ENSO oscillation, and the atmospheric heating due to moisture convergence is a dominant mechanism by which the background state is made unstable during certain periods of the calendar year. They also concluded that the next-

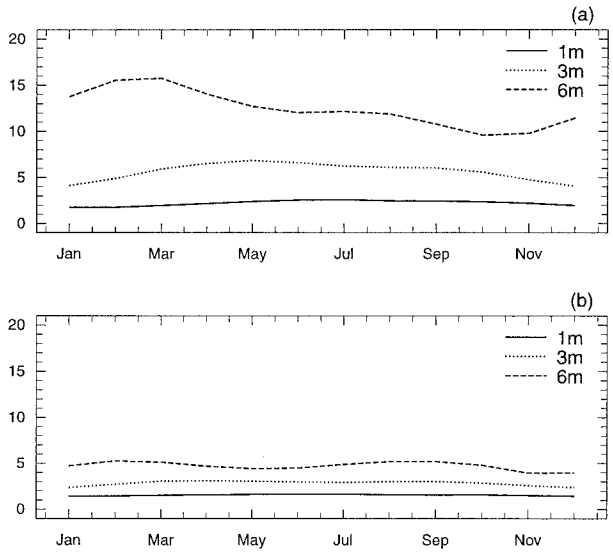

FIG. 2. (a) The first singular value and (b) second singular value of the forward tangent models about the seasonal background optimized at 1 (solid line), 3 (dotted line), and 6 (dashed line) months as functions of start month.

order seasonal effects are due to the seasonality of the background SST and ocean upwelling velocity. We suspect that the growth in summer is related to the secondary seasonal effects. During summer large mean SST gradients and strong mean upwelling work to increase the coupling strength between the ocean and atmosphere. The first singular value optimized at 6 months is largest for start months in early spring because the whole spring and summer are included; in contrast, the first singular value (optimized at 6 months) is smallest for start months in fall since the growth seasons of spring and summer are excluded.

While the first singular value is a function of start season, the first singular vector is extremely insensitive to start season as well as to optimization time. The average of the 12 singular vectors for each start month optimized at 6 months is shown in Fig. 3a, and the final pattern after 6-month evolution starting from February is shown in Fig. 3b. The amplitude of the singular vector is chosen such that after a 6-month evolution Nino-3 is about 1.3°C. It is seen that the SST field has north–south and east–west dipoles. The largest amplitude of SST is less than 0.1°C, much smaller than the typical observation error (0.2°C) (Reynolds and Smith 1994). There are convergent winds on the equator in the eastern Pacific with a maximum amplitude 0.1 m s^{-1}, also much smaller than the wind measurement error (2 m s^{-1}) (Reynolds et al. 1989). The thermocline is anomalously deep (1.5 m) along the whole equatorial belt and along the eastern coast. For the single baroclinic mode ocean model, a 1-m thermocline depth anomaly is equivalent to a 0.6-cm sea level height anomaly (Cane and Patton 1984). The typical error of sea level in tide gauge data is about 3 cm (Miller and Cane 1989). This small perturbation grows by 15-fold in 6 months (Fig. 2) and its final pattern mimics the mature phase of ENSO in ZC.

Figure 4 shows Nino-3 and Nino-4 indices of the final pattern of this singular vector as a function of start

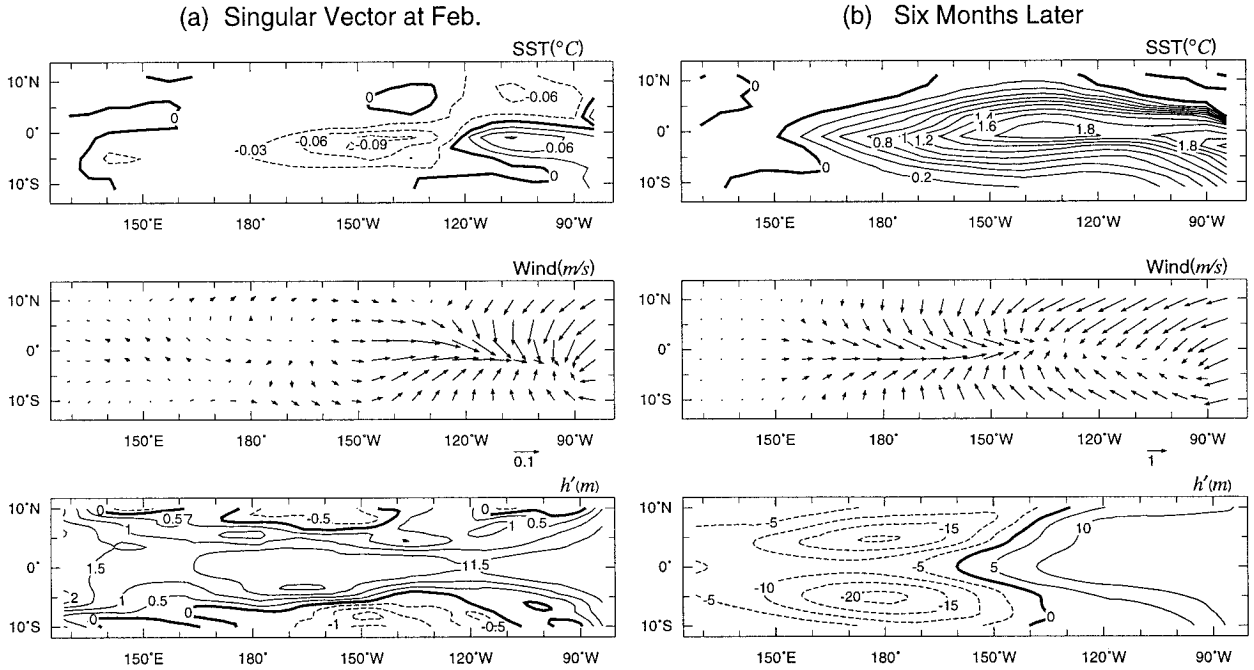

FIG. 3. (a) The average of the 12 first singular vectors of the forward tangent models about the seasonal background starting from each calendar month optimized at 6 months, and (b) its final pattern after a 6-month evolution starting from February.

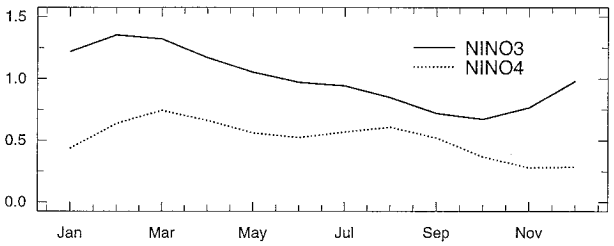

FIG. 4. The Nino-3 (solid line) and Nino-4 (dotted line) indices of the final patterns of the first singular vector shown in Fig. 3a after a 6-month evolution as functions of start month.

month. Note that the Nino-3 index has seasonal dependence similar to the first singular value, while the Nino-4 index shows two maxima of growth for start seasons early spring and early fall. This means that there are two preferred seasons in which perturbations develop in the western basin. This feature is similar to that discussed by Mantua and Battisti (1995), who found that the surges of cold anomalies propagating to the west in ZC have maximum variance in the western Pacific in spring and fall. These cold surges are the second most significant feature in ZC and are favored during the cold phases of ENSO. It is interesting to note that the two preferred seasons of maximum variability in the central and western Pacific are dictated by the seasonal background. This feature will be seen in the singular vector analysis carried out on the basis of interannually varying climatic states in the next section.

The singular vector growth given by the forward tangent model needs to be verified against that of the full nonlinear model. Because of the asymmetry in the subsurface temperature parameterization, the positive initial perturbations are expected to grow faster than the negative initial perturbations in the full nonlinear model. The forward tangent model is expected to simulate the growth of the positive perturbations better than that of the negative perturbations, since it is constructed with a symmetric subsurface temperature parameterization that assumes the parameters for positive anomalies. The first singular vector shown in Fig. 3a with positive and negative signs is used to start two full nonlinear model runs for each calendar month. The absolute values of Nino-3 in the two runs are compared with that by the forward tangent model (Fig. 5a). As expected, the positive singular vector perturbations grow much faster than the negative ones, and the simulation by the forward tangent model is closer to the positive perturbation case of the nonlinear model.

To understand which nonlinear physics contributes to the asymmetry between the two nonlinear model runs, we did several sensitivity experiments in which specifically one of the nonlinear terms was linearized. We first linearized the subsurface temperature parameterization so that it is symmetric for warm and cold anomalies. It is seen in Fig. 5b that the cold anomaly becomes bigger, and its absolute Nino-3 value is closer to that of the warm anomaly, but large differences still exist. The nonlinear advection terms underlined below in the SST equation could cause an asymmetry between the cold and warm perturbations as well:

$$\frac{\partial T'}{\partial t} = -\bar{u}T'_x - u'\bar{T}_x - \underline{u'T'_x} - \bar{v}T'_y - v'\bar{T}_y - \underline{v'T'_y} - \gamma M(\bar{w})T'_z - \gamma\{M(\bar{w} + w') - M(\bar{w})\}\bar{T}_z - \underline{\gamma\{M(\bar{w} + w') - M(\bar{w})\}T'_z}. \quad (13)$$

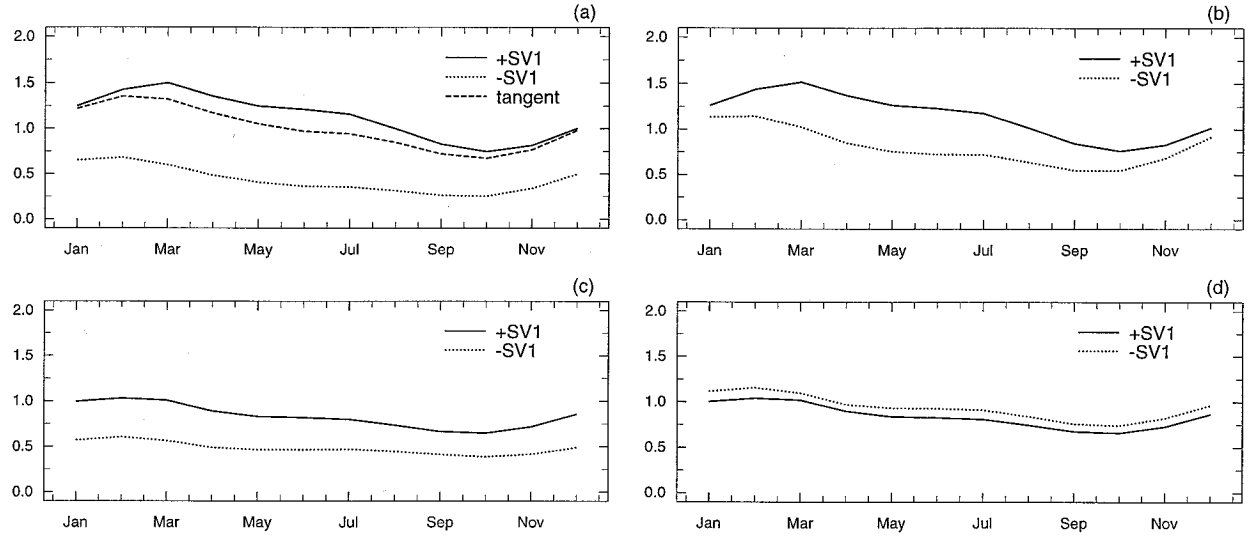

FIG. 5. (a) Comparison between the absolute Nino-3 indices of the perturbations at 6-month lead in the two nonlinear model runs started from the positive (solid line) and negative (dotted line) first singular vectors shown in Fig. 3a and that evolved by the forward tangent models (dashed line) as functions of start month; (b) same as (a) except the subsurface temperature parameterization is linearized; (c) same as (a) except the nonlinear advection terms are linearized; and (d) same as (a) except the subsurface temperature parameterization and the nonlinear advection terms are linearized simultaneously.

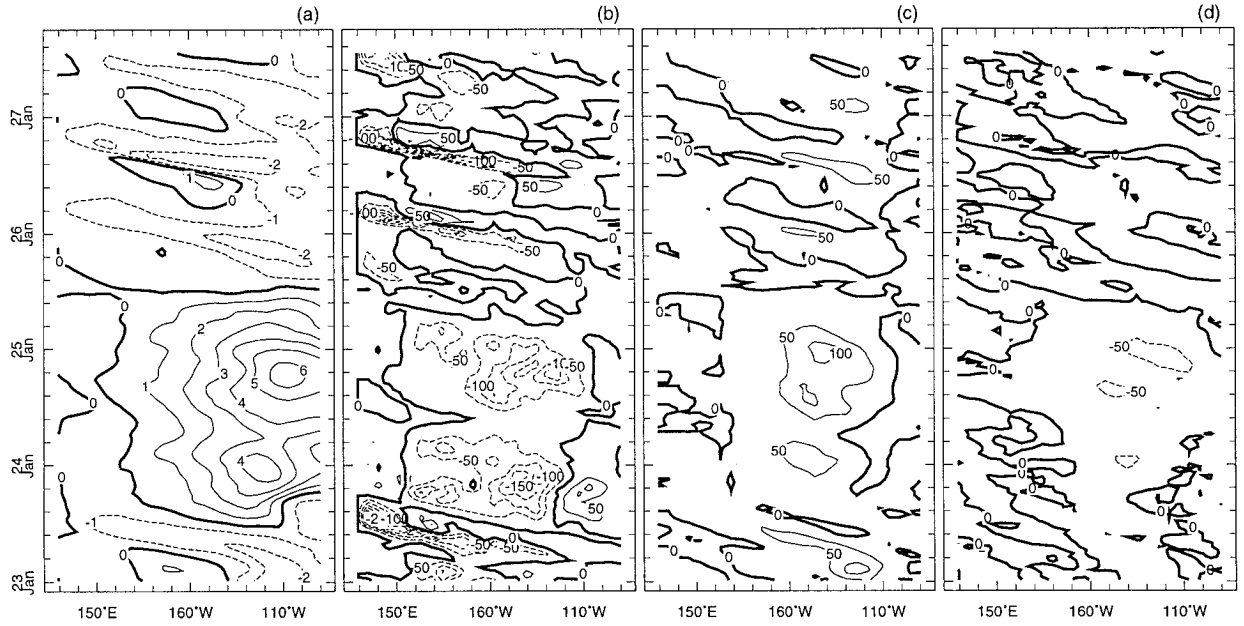

FIG. 6. (a) The SST, (b) zonal nonlinear advection, (c) vertical nonlinear advection, and (d) meridional nonlinear advection averaged over the equatorial belt (1°N–1°S) for a typical warm and cold episode in a long ZC model run. Unit for SST is degrees Celsius and units for fluxes are watts per square meter.

Here $\gamma = 0.75$ accounts for the inefficiency in the entrainment of the subsurface cold water into the surface mixed layer (cf. Zebiak and Cane 1987). Function $M(x)$ is a step function: $M(x) = x$ if $x \geq 0$; $M(x) = 0$ if $x < 0$. Figure 6 shows the nonlinear advection terms averaged in the equatorial belt (1°N–1°S) for a typical warm and cold episode in a long ZC model run. It is noticed immediately that the horizontal nonlinear advection ($-u'T'_x$ or $-v'T'_y$) is mostly a cooling and the vertical advection $[-\gamma\{M(\bar{w} + w') - M(\bar{w})\}T'_z]$ is mostly a warming. Compared with the zonal nonlinear advection, the meridional nonlinear advection is insignificant. The zonal nonlinear advection always inhibits warm SST anomalies from moving to the western Pacific but aids the westward propagation of cold SST anomalies. The vertical nonlinear advection always strengthens warm SST anomalies but diminishes cold SST anomalies in the eastern Pacific. The net effect of the nonlinear advection is to promote warm anomalies in the eastern Pacific and weaken warm anomalies in the western Pacific, while suppressing cold anomalies in the eastern Pacific and allowing propagation of cold anomalies into the western Pacific. This is consistent with the SST fields (Fig. 6a) in which the cold anomalies tend to move westward and the warm anomalies are stationary. We did a second experiment in which the nonlinear advection terms are linearized about the seasonal background and all other nonlinear terms are unchanged. The absence of vertical nonlinear advection is expected to reduce the warm anomaly and strengthen the cold anomaly in the eastern Pacific, and the absence of zonal nonlinear advection is expected to move the warm anomaly westward and reduce the westward movement of the cold anomaly. The net effect in the Nino-3 region, shown in Fig. 5c, is that the positive singular vector anomaly is indeed reduced, but the negative anomaly changes little.

Additional experiments showed that the nonlinearities associated with the atmospheric convergence feedback, vertical temperature advection, and wind stress are not important. Indeed, when the subsurface temperature parameterization and nonlinear advection terms are simultaneously linearized, while other terms are unchanged, the absolute Nino-3 indices of the positive and negative singular vector perturbations after a 6-month evolution become very similar (Fig. 5d): these two processes account for virtually all of the model's nonlinear behavior.

The discontinuity at the zero anomaly state in the subsurface temperature slope (Fig. 1) is strong (Fig 5b), but for finite anomaly states this discontinuity disappears, so the nonlinearity is less significant for interannually varying climatic states, in which the zero anomaly state is a rare event.

4. ENSO cycles

Having analyzed the perturbation growth about the seasonal background state, we next consider how perturbation growth varies with ENSO cycles. Here we examine the ENSO cycles of a long coupled model run; in Part II, we will analyze the actual ENSO cycles in the ZC forecasts over the past two decades.

As in the last section in constructing forward tangent

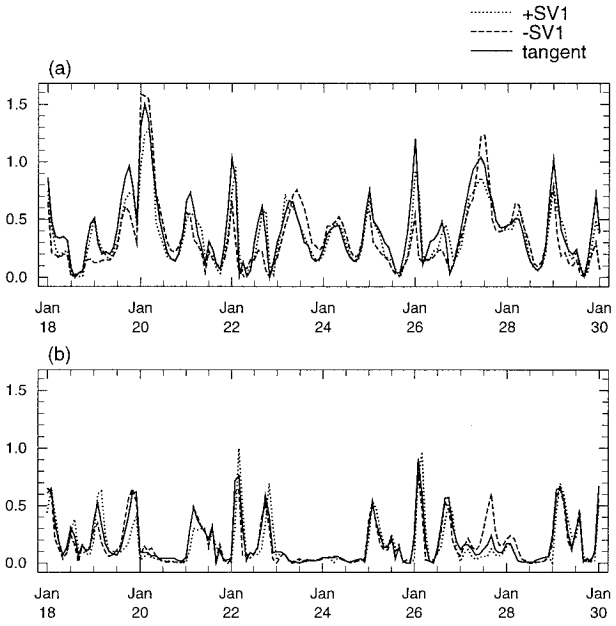

FIG. 7. Comparison of (a) the absolute Nino-3 and (b) Nino-4 indices of the perturbations at 6-month lead in the two perturbed nonlinear model runs initiated from the positive (dashed line) and negative (dotted line) first singular vector perturbations of the local forward tangent models optimized at 6 months, and that evolved by the forward tangent models (solid line) as functions of the climatic states of a 12-yr simulation from a long model run.

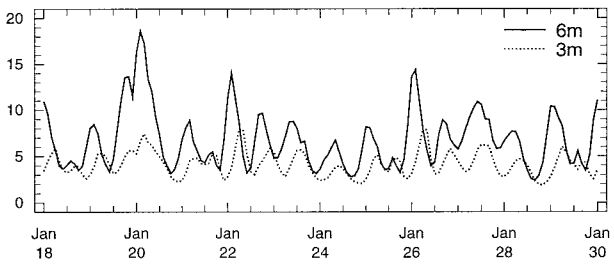

FIG. 8. The first singular values of the local forward tangent models optimized at 6 months (solid line) and at 3 months (dotted line) as functions of the climatic states of a 12-yr simulation from a long model run.

models, we have excluded the maximum SST limit of 30°C and the reinitialization of the atmospheric model from the ZC model. Singular vector analysis is performed on a 12-yr simulation from a long model run in which three ENSO cycles with slightly different timing are included. For each month of this simulation, monthly forward tangent models are constructed. We found that the first singular values of the monthly forward tangent models from positive and negative perturbations are in good agreement (differences are less than 5%). The forward tangent models for a 6-month duration are the multiplication of 6 monthly forward tangent models.

For verification of the forward tangent models, the first singular vector of each local forward tangent model optimized at 6 months with both positive and negative signs is used to perturb each initial state, from which two perturbed nonlinear model runs are carried out. The differences between the perturbed nonlinear model runs and the control run are called perturbations. The initial amplitude of the perturbations is equal to that in Fig. 3a, as measured by the energy norm. This amplitude is small enough that the nonlinearities in the evolution of the perturbations are generally small. The absolute Nino-3 and Nino-4 indices of the perturbations in the two perturbed nonlinear model runs at 6-month lead are compared with those evolved by the forward tangent models (Figs. 7a and 7b). It is seen that from time to time the Nino-3 and Nino-4 indices of the positive and negative perturbations differ appreciably, indicating nonlinearity. Generally speaking, the perturbation growth is linear and the forward tangent models simulate the perturbation growth of the full nonlinear model reasonably well.

The first singular value optimized at 3 months is compared with that optimized at 6 months in Fig. 8. From time to time the first singular value optimized at 3 months is comparable with that optimized at 6 months, and occasionally the former is even larger than the latter. This is in contrast with Fig. 2, where the first singular value optimized at 6 months is always larger than the first singular value optimized at 3 months. The results indicate that the ENSO cycles have modified the perturbation growth of the seasonal background significantly.

The first singular vectors are generally insensitive to initial time and optimization time. For example, we found that the first singular vectors optimized at 3 months are only slightly suboptimal for 6-month growth. Also, the average of the 12 singular vectors of the forward tangent models about the seasonal background (Fig. 3a) grows almost as fast as the 6-month optimized first singular vector (not shown). However, during cold phases, for example, around January of years 22, 26, and 29, the first singular vectors are somewhat different. Figure 9 shows the first singular vector optimized at 6 months starting from January of year 26. It is seen that the wind field is centered more in the east compared with that of Fig. 3a and the thermocline depth is negative in the far eastern Pacific as opposed to that of Fig. 3a. By examining the thermodynamics in the perturbation growth, we found that during this period the system is insensitive to thermocline depth perturbations because of the large negative thermocline depth anomalies (Fig. 1).

For examining the variability in (6 month) optimal growth during ENSO cycles, Fig. 10 shows the SST and thermocline depth anomalies averaged over the equatorial belt (1°N–1°S) for the 12-yr simulation, together with the averaged Nino-3 and Nino-4 indices of the positive and negative perturbations in the two perturbed nonlinear model runs. For comparison, the perturbation growth about the seasonal background state is also shown (Fig. 10c). It is seen that the ENSO cycles mostly

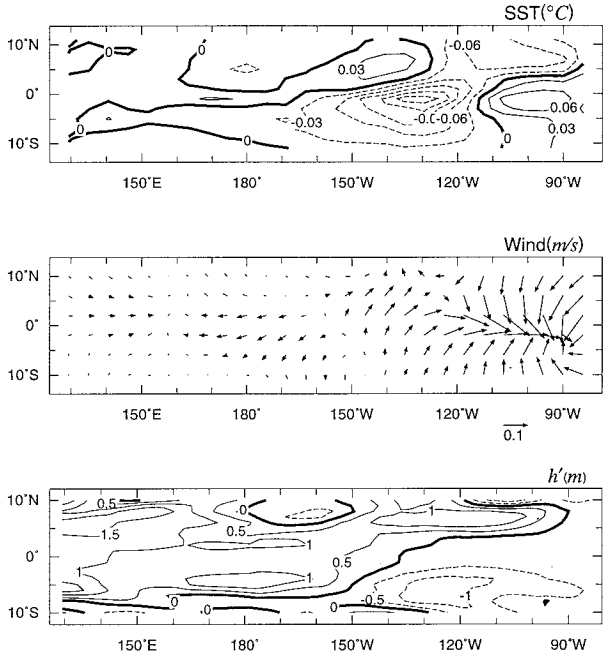

FIG. 9. The first singular vector of the local forward tangent model optimized at 6 months starting from January of year 26.

suppress the growth rate of the seasonal background. During the warm phase of ENSO, the growth rate is a strong function of start season. Generally speaking, at the onset of warm events, typically occurring during spring, there is a maximum of growth rate; then a minimum in later fall, followed by another maximum in spring during the mature phase; then a minimum in fall followed by a maximum in early spring during the decay phase. However, the growth rate may be greatly modulated by interannual anomalies. For example, in the warm phase starting from February of year 20, the growth rate is the largest of the whole simulation and is significantly larger than that of the other two warm phases. In the last section, we pointed out that when the thermocline depth anomaly is slightly positive the system is most unstable (Fig. 1). When this happens in spring, the atmosphere has its strongest response to the SST anomalies, as the ITCZ is closest to the equator, and this is the case in February of year 20 (Figs. 10a and 10b). For the other two warm events, the thermocline depth anomaly in the eastern Pacific changes sign from negative to positive in fall, and the growth rate of the system is significantly reduced (Figs. 10b and 10c). During the cold phases of ENSO, the perturbations tend to spread to the western Pacific, and two maximum growth seasons are seen: spring and fall (Fig. 10c).

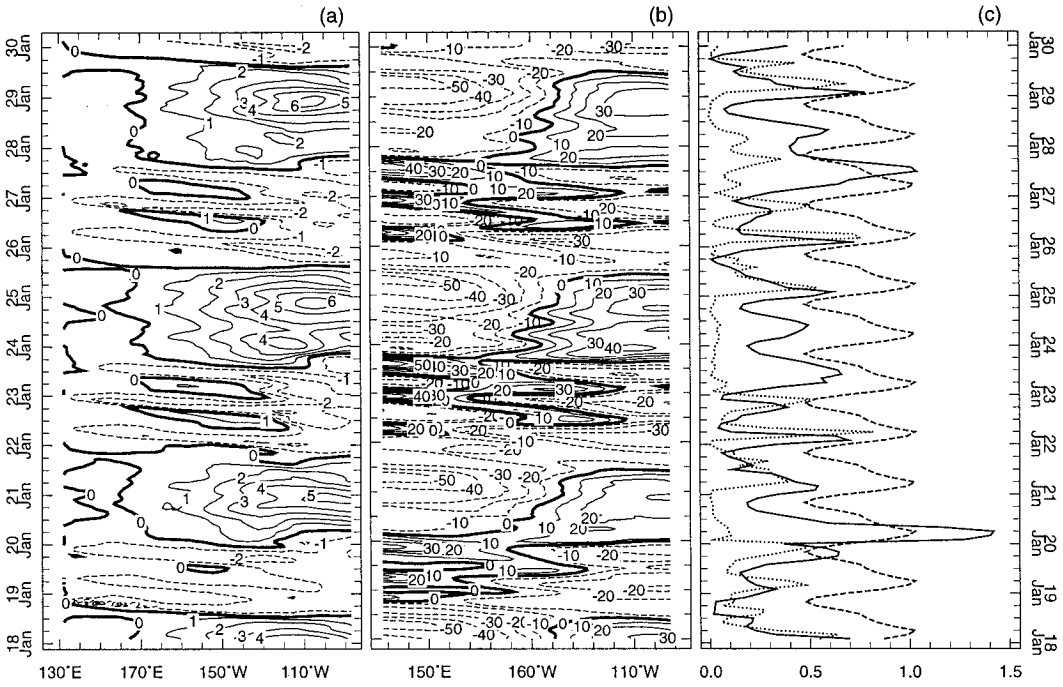

FIG. 10. Time–longitude contour plots of (a) the SST and (b) thermocline depth anomaly averaged over the equatorial belt (1°N–1°S) of a 12-yr simulation from a long model run. (c) Comparison between the averaged absolute Nino-3 (solid line) and Nino-4 (dotted line) indices of the perturbations at 6-month lead in the two perturbed nonlinear model runs initiated with the positive and negative first singular vector perturbations of the local forward tangent models optimized at 6 months as functions of the climatic states of a 12-yr simulation from a long model run. The averaged absolute Nino-3 indices of the positive and negative singular vector perturbations in Fig. 5a are shown (dashed line), repeated every year, for comparison.

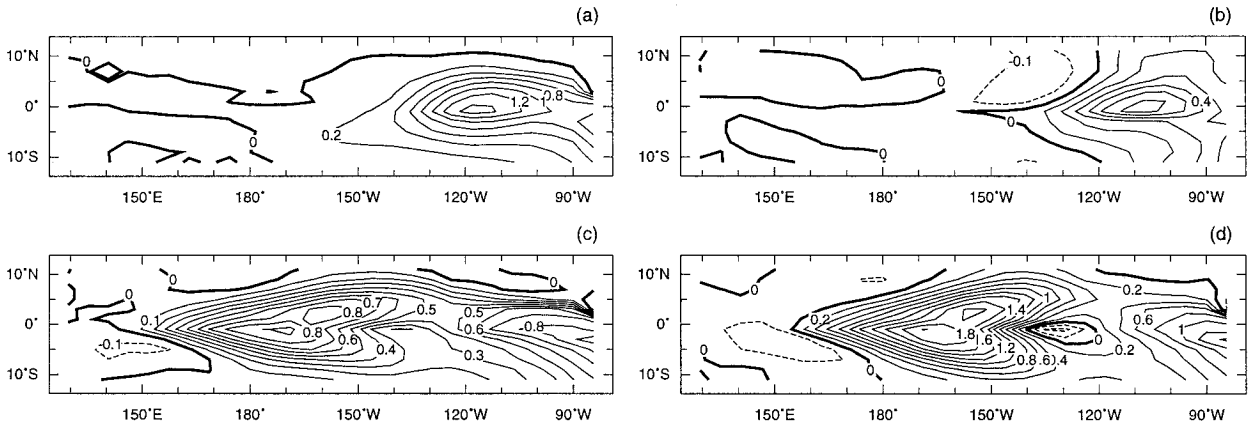

FIG. 11. The final SST patterns of the first singular vectors of the local forward tangent models optimized at 6 months after a 6-month evolution starting from (a) April of year 23, (b) October of year 23, (c) February of year 25, and (d) February of year 26.

The final patterns of the first singular vectors after a 6-month evolution vary. For example, starting from April of year 23, the first singular vector grows by about eightfold and its final SST field is confined to the eastern Pacific (Fig. 11a). In contrast, starting from October of year 23, the first singular vector does not grow much at all (Fig. 11b). During the decay phase of warm events, the first singular vector often has a moderate growth rate and its final pattern spans both the eastern and western Pacific (Fig. 11c). Examining the Nino-3 and Nino-4 indices in Fig. 10c, it is found that during the onset and mature phases of ENSO, the final pattern of the first singular vector is mostly confined to the eastern Pacific; while during the decay phase of ENSO, the final pattern of the first singular vector spans the western Pacific as well as the eastern Pacific. During the cold phases of ENSO, there are two preferred growth seasons, and there is a propagation feature clearly shown by the phase shift in the Nino-3 and Nino-4 indices (Fig. 10c). For example, starting from February of year 26, the first singular vector propagates to the west, and its final SST pattern has most variance in the central and western Pacific (Fig. 11d). The fast westward propagation is due to the strong zonal advection associated with the large SST gradients at the western edge of the perturbations. These westward-moving perturbations are related to the instability of the surface layer and do not seem to have counterparts in reality (Mantua 1994).

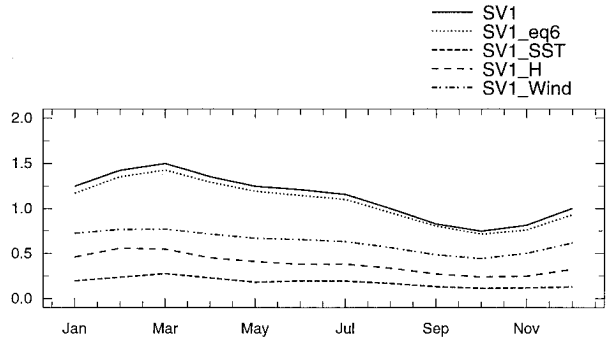

FIG. 12. Comparison between the Nino-3 indices of the perturbations after a 6-month evolution by the full nonlinear model initiated with all the fields of the first singular vector shown in Fig. 3a (solid line), the fields in the equatorial belt (6°N–6°S) (dotted line), the SST field only (dashed line), the thermocline field only (long-dashed line), and the wind field only (dot–dash line).

5. Sensitivity of growth rate to variables and norm definition

The first singular vector structure shown in Fig. 3a is dependent of norm definition. The energy norm used in this study is arbitrary, under which initial perturbations are white in the multivariate EOF space. The natural question is what the contribution of each field of the first singular vector is to the optimal growth. First, we found that the near-equatorial perturbations (6°N–6°S) account for almost all of the growth in Nino-3 (Fig. 12). This is understood since it is only in the equatorial belt that the ocean and atmosphere are strongly coupled on relatively short timescales. For each calendar month the nonlinear model was integrated for 6 months starting from one of the fields of the first singular vector shown in Fig. 3a, while the rest of the fields were set to zero. We found that the wind field contributes a little more than half of the total growth, the thermocline field contributes about one-third, and the SST field contributes only one-tenth (Fig. 12). The variance distribution among the fields of the first singular vector is as follows. The variance (normalized) of the oceanic variables (H, U, and V) of the first singular vector [refer to Eqs (1) and (2)] is 2.9 times of that of the SST and 1.9 times of that of the winds. This indicates that under the energy norm the variance of each field of the first singular vector is selected in such a way that the fields of wind and thermocline depth contribute more to optimal growth than the SST field does.

Chen et al. (1997) used the Battisti version of the ZC

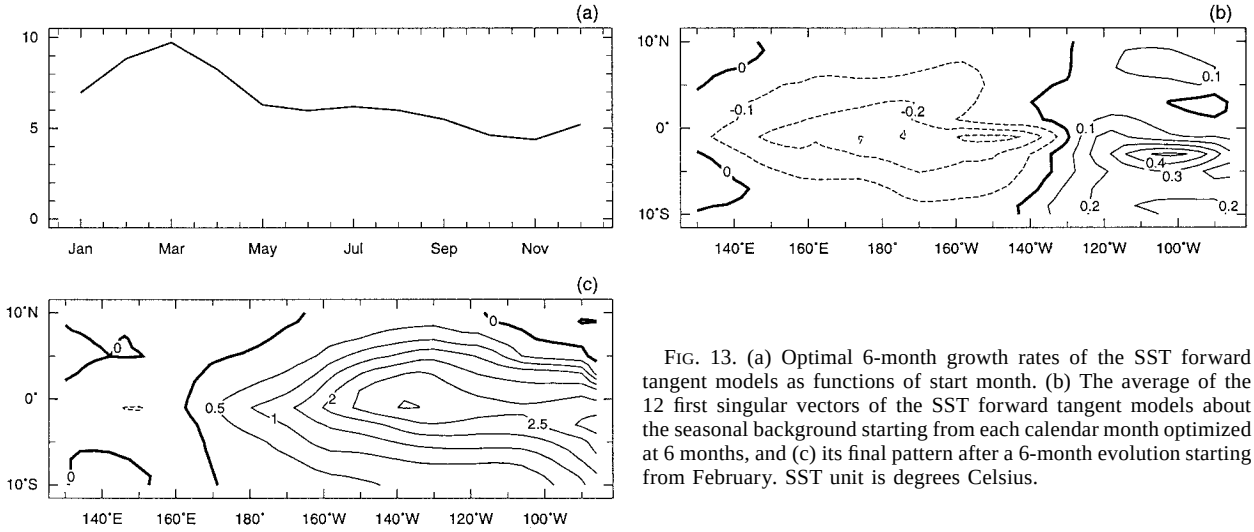

FIG. 13. (a) Optimal 6-month growth rates of the SST forward tangent models as functions of start month. (b) The average of the 12 first singular vectors of the SST forward tangent models about the seasonal background starting from each calendar month optimized at 6 months, and (c) its final pattern after a 6-month evolution starting from February. SST unit is degrees Celsius.

model and applied the Lorenz method to the SST field, that is, by perturbing SST in each grid point and running the full nonlinear model forward for several months to get a matrix connecting initial to final SST perturbation fields. With this forward tangent model of SST, they calculated singular vectors maximizing SST variance subject to an initial perturbation in the SST field. It is noticed that our SST field of the first singular vector about the seasonal background (Fig. 3a) is somewhat different from that of Chen et al. (1997). Since the norm definitions are different in Chen et al. and our paper, and also the two models differ in many ways (see Mantua 1994 for details), the differences in singular-vector structures are not surprising. However, it is interesting to know whether the result of Chen et al. is repeatable if we use a similar norm definition. In the EOF space of SST (with 37 modes), forward tangent models connecting initial to final SST perturbation fields about the seasonal background were constructed. The Lorenz method is applied much the same as in the multivariate EOF space: given a small perturbation of an SST EOF, the full nonlinear model (with three modifications: no 30°C limit, no reinitialization, and symmetric subsurface temperature parameterization) is run for several months, and the final SST perturbation field is projected onto the 37 EOFs. Then a forward tangent model in the 37 SST EOF space connecting initial to final SST perturbations is obtained. It is noticed that a τ month transition matrix of SST is not equivalent to a multiplication of τ monthly transition matrices of SST. This is because the monthly SST forward tangent model does not describe the ocean dynamics, while the latter has a delay effect on SST. Positive and negative perturbations are used to construct two forward tangent models, and the first singular values of the two 6-month transition matrices differ by less than 8%. The forward tangent models are found to simulate the singular-vector perturbation growth within the nonlinear model quite well.

The first singular value optimized at 6 months is shown in Fig. 13a as a function of start month. It is seen that the seasonality of the growth rate is stronger than that in Fig. 2a and the overall growth rate is smaller. This implies that wind and thermocline perturbations grow faster than SST perturbations. We will come back to this point later. As in the earlier study, the first singular vector of the SST forward tangent model is insensitive to initial month. The average of the 12 singular vectors for each start month optimized at 6 months is shown in Fig. 13b, and its final pattern after a 6-month evolution starting from February is shown in Fig. 13c. Compared with the SST pattern in Fig. 3a, the cold patch in the central and western Pacific is larger, and the meridional extent of the warm patch is larger. This SST pattern is much closer to that of Chen et al. (1997).

The wind pattern associated with the optimal SST pattern (Fig. 13b) can be derived from the atmospheric model. Starting from either the SST pattern or the associated wind pattern, the nonlinear model is integrated for 6 months. The growth rate for the SST pattern is measured by the ratio of the energy norm at 6-month lead to the initial variance (normalized) of SST; the growth rate for the wind pattern is measured by the ratio of the energy norm at 6-month lead to the initial variance (normalized) of the corresponding winds. The energy norm in physical space is the sum of the variance (normalized) of each field. The normalization is that presented in Eq. (1). Figure 14 shows that the growth rate for the SST is only two-thirds of that for the winds. This suggests that the system is more sensitive to the variance of the winds (normalized) than the variance of the SST (normalized).

We can interpret this experiment practically. If we

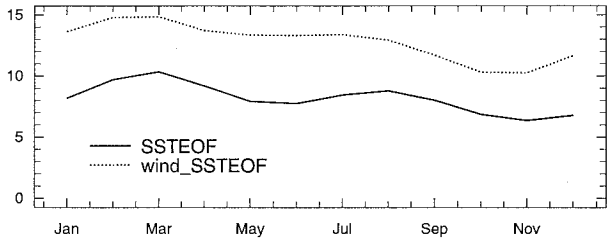

FIG. 14. Comparison of the growth rates measured by the ratio of the energy norm at 6-month lead to that at initial time as functions of start month. The initial perturbations are the SST field in Fig. 13b (solid line) and the wind field derived from this SST pattern (dashed line).

scale the final pattern to have a Nino-3 index of 2.1°C, the initial optimal SST pattern is that shown in Fig. 13b, and the corresponding wind pattern is derived from the atmospheric model (not shown). We found that the maximum SST perturbation is 0.5°C and the maximum westerly perturbation on the equator is 0.3 m s^{-1}. If the SST observation error is 0.3°C (Reynolds and Smith 1994) and the wind measurement error is 2 m s^{-1} (Reynolds et al. 1989), it is obvious that the wind errors are more likely to be problematic than the SST errors.

6. Summary and conclusions

The transient growth in a non-self-adjoint system has found many applications in ocean and atmosphere systems (Farrell 1989; Blumenthal 1991; Palmer et al. 1994). A system with a spatially varying basic state, or one with a different coupling strength between subsystems, is generally non-self-adjoint; thus, almost every realistic system is. Blumenthal (1991) first pointed out that the ENSO system in ZC is a non-self-adjoint system in which fast transient growth is an important source of error in forecasts. In this paper, forward tangent models about the seasonal background state and interannually varying ENSO states were constructed in a multivariate EOF space, and the singular vectors and singular values were explored.

For the seasonal background state, the first singular value is much larger than the second singular value. The first singular value optimized at 6 months is largest for early (northern) spring starts. This is because the background wind convergence field is largest in early spring when the ITCZ is closest to the equator, and the subsequently enhanced atmospheric heating through the convergence feedback destabilizes the coupled system significantly (Tziperman et al. 1997). During the summer, high SST gradient and mean upwelling are probably the main factors for subsequent fast growth (Tziperman et al. 1997). So the optimal growth of 6 months is largest for early spring starts when the spring and summer are included, while it is smallest for fall starts since the growth seasons of spring and summer are excluded.

The first singular vector is insensitive to start season and is characterized by north–south and east–west SST dipoles, convergent winds on the equator in the eastern Pacific, and a deepened thermocline in the whole equatorial belt (Fig. 3a). It was noticed that the SST, wind, and thermocline fields of the first singular vector are not necessarily in dynamical balance and are dependent on norm definition. Under the energy norm the variance of each field of the first singular vector is selected in such a way that the wind and thermocline fields contribute more to the optimal growth than the SST field. The first singular vector might appear as initial errors in analysis, which usually do not satisfy dynamic constraints. The energy norm used in this study is only the first attempt to analyze optimal growing initial errors. In Part II, we will exam the initial error fields of the ZC forecasts and study what is the appropriate norm for describing initial error growth.

Three continuous ENSO cycles in a 12-yr simulation of a long-coupled model run were subject to singular vector analysis. Each cycle has similar amplitude, structure, and period but has somewhat different timing. The optimal growth is generally much smaller than that due to the seasonal background alone. This is because the system is most sensitive to thermocline depth perturbations at the zero anomaly state (Fig. 1) and because this state is rarely seen in simulation. However, occasionally, when the thermocline depth anomaly changes sign from negative to positive in early spring, the optimal growth can be larger than that of the seasonal background (February of year 20 in Fig. 10c).

The first singular value is dominant, and the first singular vectors of the local forward tangent models do not vary much with initial states. The wind field of the first singular vectors often contributes the most to the growth rate through the convergent winds on the equator in the eastern Pacific.

The growth rate for warm events is predominantly seasonal. For 6-month optimal growth there is a maximum in spring during the onset of a event, then a minimum in late fall, then a second maximum in the following spring, then a minimum in fall and a third maximum in the following spring during the decay phase of a event (Fig. 10c). For the first two maxima, the final patterns of the first singular vector perturbations are mainly confined to the eastern Pacific (Figs. 11a and 11b), while for the last peak during the decay phase of a warm event the final patterns of the first singular vectors span the whole Pacific (Fig. 11c). The above seasonal growth rate breaks down for cold events. During the onset of a cold event, there is little growth; while during the mature phase of a cold event the growth rate has two peaks, in spring and fall. The first singular vector perturbations move westward quickly and are related to the instability of the surface layer (Mantua 1994).

Our results are similar in some respects to those of Chen et al. (1997), in which the Battisti version of the

ZC model (Battisti 1988) was studied. The Battisti model differs from the ZC model in many ways; in particular, its subsurface temperature is made to be twice as sensitive to thermocline depth anomaly as that in ZC (see Mantua 1994 for details). Its ENSO cycles in a long model run are very regular in contrast to the chaotic behavior of the ZC model. Chen et al. constructed forward tangent models in physical space and chose to optimize SST variance. The wind pattern corresponding to their optimal SST pattern is somewhat similar to the wind pattern of the first singular vector shown in Fig. 3a. They also found that the first singular vector is not sensitive to initial time and optimization time. However, the second significant feature in ZC, related to the westward moving surges in the cold phase of ENSO, is absent in the Battisti model. Therefore the rich variability of the final patterns of the first singular vectors for the ZC model is absent in the Battisti model (Chen et al. 1997).

Forward tangent models in multivariate EOF space have the advantage of optimizing all model variables simultaneously. However, the norm definition could selectively emphasize some variables over others. The energy norm used in the paper has emphasized the wind and thermocline fields over the SST and other variables. Recently Thompson (1997) further analyzed the optimal growth in the Battisti model and discussed the SST optimal, thermocline depth optimal, and the full optimal including all variables. His thermocline optimal is very similar to the thermocline pattern in Fig. 3a. Thompson presented a thorough comparison between the three related works and discussed the relationship between singular vector structures and norm definition. The goal of singular vector analysis is to find the optimal growing errors in analyses. Assuming analyses errors in SST field alone is unrealistic. An appropriate norm definition that describes a white error field is essential. With a white initial error covariance, optimal growth would describe the dominant initial error growth. In Part II, we will examine how well the energy norm used in this paper describes the initial error fields of the ZC forecasts.

Moore and Kleeman (1996) found somewhat different singular vector structures using the coupled model at the Australian Bureau of Meteorology Research Center. This is not surprising since their model has a different atmospheric component and quite different ocean thermodynamics. Their singular vectors start from the western Pacific with a deepened thermocline, and relatively ''noisy'' SST and wind fields, and then move to the central Pacific and get amplified through penetrative convection. Since in their model the subsurface influence is confined to the eastern Pacific, but the atmospheric heating (penetrative convection) is in the central Pacific, ocean wave propagation is essential for their perturbation growth. They concluded that only ocean memory is important for singular vector growth. However, in the ZC system, a portion of the wind response is directly related to the local SST anomaly, and as a result, the atmosphere and ocean are strongly coupled in the eastern Pacific. So wave propagation is not so important for fast perturbation growth, although it is crucial for interannual variability through the ''delayed oscillator'' mechanism. It has been shown that boundary layer processes are important in the eastern Pacific (Lindzen and Nigam 1987). Given that this model has a reasonable forecast skill of ENSO for up to 2-yr lead, it is plausible that the perturbation growth explored here with singular vector analysis is realistic.

In summary, singular vector analysis is a useful tool for studying the perturbation growth of the ENSO system. It helps in understanding the fundamental physics in ZC. In Part II, this tool will be used to study the actual ZC forecasts of ENSO in the past two decades. It is probable that sophisticated GCMs or other intermediate models have different singular vector structures and different optimal growth rates. Applying a singular vector analysis to those models is an important step toward understanding these models and their predictions.

Acknowledgments. This research has been supported by the TOGA Program on Seasonal to Interannual Prediction through National Oceanic and Atmospheric Administration Grant NA16RC0432-03. We would like to thank Tim Palmer and Zoltan Toth, who read our draft carefully and gave us helpful comments. Especially we thank the anonymous reviewers who helped us make this paper more concise and more understandable.

REFERENCES

Battisti, D. S., 1988: The dynamics and thermodynamics of a warming event in a coupled tropical atmosphere–ocean model. *J. Atmos. Sci.,* **45,** 2889–2919.

Blumenthal, M. B., 1991: Predictability of a coupled ocean–atmosphere model. *J. Climate,* **4,** 766–784.

Buizza, R., and T. N. Palmer, 1995: The singular-vector structure of the atmospheric general circulation. *J. Atmos. Sci.,* **52,** 1434–1456.

Cane, M. A., and R. J. Patton, 1984: A numerical model for low-frequency equatorial dynamics. *J. Phys. Oceanogr.,* **14,** 1853–1863.

——, S. E. Zebiak, and S. C. Dolan, 1986: Experimental forecasts of El Niño. *Nature,* **321,** 827–832.

Chen, Y.-Q., D. S. Battisti, T. N. Palmer, J. Barsugli, and E. S. Sarachik, 1997: A study of the predictability of tropical Pacific SST in a coupled atmosphere–ocean model using singular vector analysis: The role of the annual cycle and the ENSO cycle. *Mon. Wea. Rev.,* **125,** 831–845.

Farrell, B., 1989: Optimal excitation of baroclinic waves. *J. Atmos. Sci.,* **46,** 1193–1206.

Ji, M., A. Kumar, and A. Leetmaa, 1994: An experimental coupled forecast system at the National Meteorological Center, some early results. *Tellus,* **46A,** 398–418.

Lacarra, J.-F., and O. Talagrand, 1988: Short-range evolution of small perturbations in a barotropic model. *Tellus,* **40A,** 81–95.

Latif, M., T. P. Barnett, M. A. Cane, M. Flügel, N. E. Graham, H. von Storch, J.-S. Xu, and S. E. Zebiak, 1994: A review of ENSO prediction studies. *Climate Dyn.,* **9,** 167–179.

Lindzen, R. S., and S. Nigam, 1987: On the role of sea surface

temperature gradients in forcing low-level winds and convergence in the tropics. *J. Atmos. Sci.,* **44,** 2418–2436.

Lorenz, E. N., 1965: A study of the predictability of a 28-variable atmospheric model. *Tellus,* **3,** 321–333.

Mantua, N. J., 1994: Numerical modeling studies of the El Niño–Southern Oscillation. Ph.D. dissertation, University of Washington, 139 pp. [Available from University Microfilms, 1490 Eisenhower Place, P.O. Box 975, Ann Arbor, MI 48106.]

——, and D. S. Battisti, 1995: Aperiodic variability in Zebiak–Cane coupled ocean–atmosphere model: Air-sea interactions in the western equatorial Pacific. *J. Climate,* **8,** 2897–2927.

McCreary, J. P., and D. L. T. Anderson, 1991: An overview of coupled ocean–atmosphere models of El Niño and Southern Oscillation. *J. Geophys. Res.,* **96,** 3125–3150.

Miller, R. N., and M. A. Cane, 1989: A Kalman filter analysis of sea level heights in the tropical Pacific. *J. Phys. Oceanogr.,* **19,** 773–790.

Molteni, F., and T. N. Palmer, 1993: Predictability and finite-time instability of the northern winter circulation. *Quart. J. Roy. Meteor. Soc.,* **119,** 269–298.

——, R. Buizza, T. Palmer, and T. Petroliagis, 1996: The ECMWF ensemble prediction system: Methodology and validation. *Quart. J. Roy. Meteor. Soc.,* **122,** 73–119.

Moore, A. M., and R. Kleeman, 1996: The dynamics of error growth and predictability in a coupled model of ENSO. *Quart. J. Roy. Meteor. Soc.,* **122,** 1405–1446.

Mureau, R., F. Molteni, and T. N. Palmer, 1993: Ensemble prediction using dynamically-conditioned perturbations. *Quart. J. Roy. Meteor. Soc.,* **119,** 299–323.

Palmer, T. N., R. Buizza, F. Molteni, Y.-Q. Chen, and S. Corti, 1994: Singular vectors and predictability of weather and climate. *Philos. Trans. Roy. Soc. London, Ser. A,* **348,** 459–475.

Reynolds, R. W., and T. M. Smith, 1994: Improved global sea surface temperature analyses using optimum interpolation. *J. Climate,* **7,** 929–948.

——, K. Arpe, C. Gordon, S. P. Hayes, A. Leetmaa, and M. J. McPhaden, 1989: A comparison of tropical Pacific surface wind analyses. *J. Climate,* **2,** 105–111.

Strang, G., 1988: *Linear Algebra and Its Applications.* Harcourt Brace Jovanovich, 442 pp.

Thompson, C. J., 1997: Initial conditions for optimal growth in a coupled ocean–atmosphere model of ENSO. *J. Atmos. Sci.,* in press.

Tziperman, E., S. E. Zebiak, and M. A. Cane, 1997: Mechanisms of seasonal–ENSO interaction. *J. Atmos. Sci.,* **54,** 61–71.

Xue, Y., M. A. Cane, S. E. Zebiak, and B. Blumenthal, 1994: On the prediction of ENSO: A study with a low-order Markov model. *Tellus,* **46A,** 512–528.

——, ——, ——, and T. N. Palmer, 1997: Predictability of a coupled model of ENSO using singular vector analysis. Part II: Optimal growth and forecast skill. *Mon. Wea. Rev.,* **125,** 2057–2073.

Zebiak, S. E., 1986: Atmospheric convergence feedback in a simple model for El Niño. *Mon. Wea. Rev.,* **114,** 1263–1271.

——, and M. A. Cane, 1987: A model El Niño–Southern Oscillation. *Mon. Wea. Rev.,* **115,** 2262–2278.